

# Integrated Plasmonic Gold Nanoparticle Dimer Array for Sustainable Solar Water Disinfection

Daniel Krueger, Ashley Graves, Yanan Chu, Jianhan Pan, Somin Eunice Lee,\* and Younggeun Park\*

Cite This: *ACS Appl. Nano Mater.* 2023, 6, 5568–5577

Read Online

ACCESS |



Metrics &amp; More



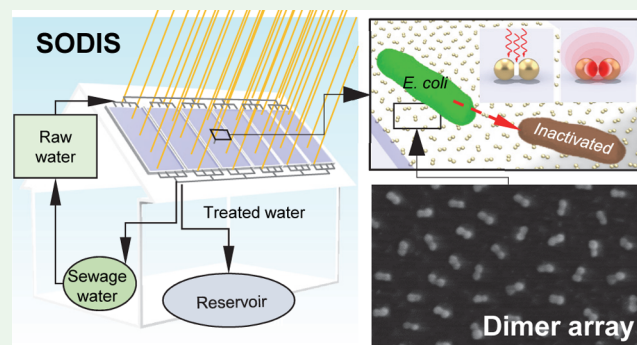
Article Recommendations



Supporting Information

**ABSTRACT:** Plasmonic nanostructures, functioning as nano-antenna reactors to highly focus light and efficiently convert it into thermal/chemical energy, have a significant potential for sustainable solar water disinfection (SODIS). A high-density plasmonic nanogap-based reactor array opens a way of maximizing the photothermal effect, but achieving uniformity and large density in such a technology while scaling up remains challenging. In this study, we provide an integrative plasmonic dimer array (hPDA) that is uniform and has high density ensuring significantly enhanced SODIS performance. The hPDA is constructed by a combined fabrication of the self-assembled monolayer and block copolymer lithography approaches. This combination leads to a two-dimensional hexagonal array of the Au dimer structures consisting of a 1.3 nm nanogap. The uniformity and high density of nanogaps of the hPDA result in the physically and optically stabilized dimer array, which allows strong light focusing and a rapid and highly efficient harvesting of photothermal energy in the visible region. Finally, the integrated hPDA with an optofluidic reactor enables 5-fold enhanced *Escherichia coli* (*E. coli*) disinfection. We anticipate that the hPDA will be useful in the scalable sustainable energy and environmental process that converts solar energy.

**KEYWORDS:** plasmonic dimer array, photothermal effect, solar water disinfection, sustainable technology, ordered plasmonic structure



## INTRODUCTION

One of the grandest challenges in the current society is to sustain the quality of life by overcoming the energy and environmental issues simultaneously since energy consumption and environmental remediation usually stand in a trade-off with each other. While more than 2 billion people's life quality in the world is impacted by waterborne illnesses (e.g., diarrheal diseases)<sup>1,2</sup> causing over half a million deaths each year, highly intensive energy resources are in demand to mitigate such water contamination issues, especially in developing and undeveloped countries. In this circumstance, solar disinfection (SODIS) in water control and treatment has garnered great attention owing to easy access, abundance, and cleanliness.<sup>3–5</sup> Mainly, as a decentralized approach, SODIS utilizes the converted thermal energy from sunlight via optical reactors. Since water has a high heat capacity and is a poor absorber of solar irradiation, the temperatures necessary to achieve synergistic inactivation by heat and sunlight are rarely achieved in conventional SODIS approaches; SODIS suffers from poor performance in many low-resource societies, which is linked to the length of time, the necessity for a clean, intact, and less-systematic operation methods.<sup>5,6</sup>

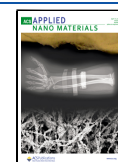
To overcome these issues, the incorporation of nanostructures in SODIS, allowing highly efficient sustainable processes, has been studied.<sup>7,8</sup> Several photothermal materials, such as

metallic nanoparticles<sup>9–14</sup> and carbon,<sup>8,15,16</sup> boost the ability to localize heat by efficiently absorbing incoming photons. In particular, recently, significant efforts have been demonstrated in the incorporation of localized surface plasmon resonance (LSPR) nanostructures into SODIS.<sup>7,17,18</sup> Photothermal effect in the plasmonic nanostructure has been demonstrated as a potentially promising approach for SODIS since it allows the highly focused collection of sunlight and the straightforward energy conversion into heat.<sup>19</sup> According to the plasmon decay mechanism, the photothermal effect in the LSPR nanostructure stems from the amplified movement of the conduction electrons,<sup>20–32</sup> and this results in the frequency of collisions with the lattice atoms.<sup>11,19,33,34</sup> This lattice–lattice vibration in the nanostructure leads to the photothermal effect.<sup>11,33–36</sup> The generated heat power therefore directly relies on the light absorption which is a function of shape, size, and composition of the plasmonic nanostructure, especially with sub-nano-/nano-features. Researchers have investigated a variety of

Received: January 3, 2023

Accepted: March 4, 2023

Published: March 22, 2023



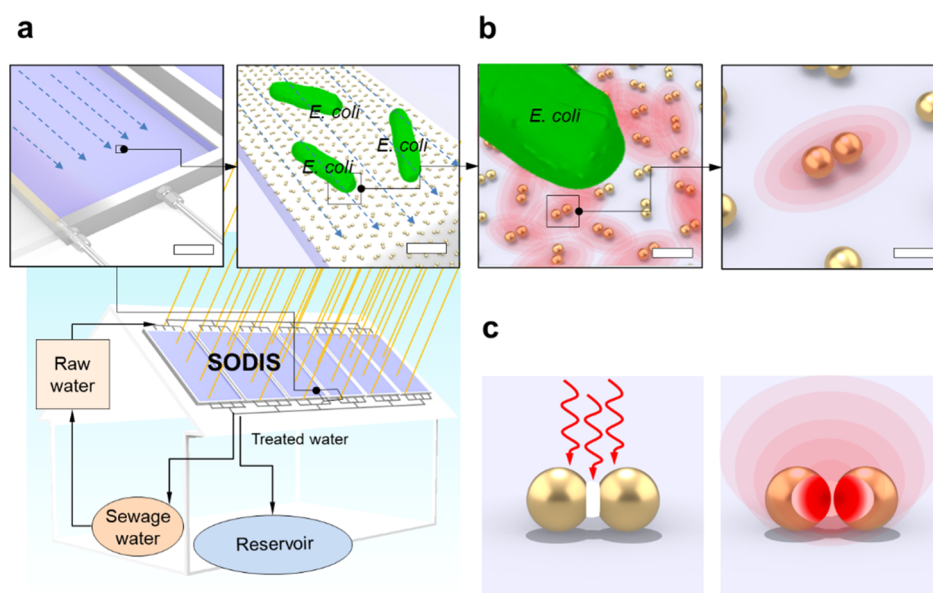


**Figure 1.** SODIS approach enabled by the highly enhanced photothermal effect of the high-density and uniform plasmonic dimer array in the optofluidic panel. (a) The integrated SODIS optofluidic panels prospectively equipped onto a roof in a residential place (scale bar in the right scheme = 10 cm and scale bar in the left scheme = 1  $\mu\text{m}$ ). The SODIS optofluidic panel is an integrated optofluidic reactor with hPDA that maximizes the interaction between incident light and water. As a thermal energy storage system, the hPDA results in very efficient and long-term water heating. (b) The light-induced thermal energy generation from the hPDA enables us to inactivate water pathogens in the contaminated water (scale bar in the right scheme = 500 nm and scale bar in the left scheme = 100 nm). (c) The highly focused electromagnetic field in the nanogap antennas and the highly enhanced photothermal effect in the nano-reactor of the hPDA lead to collective heating for SODIS.

plasmonic nanostructures, including colloidal nanoparticles, a nanostructure-deposited substrate, a nanostructured packed bed, and batch reactors, to obtain the greatly improved photothermal effect.<sup>12,34,36–38</sup> However, due to the lack of precise control over nano-features, such designs are frequently associated with difficulties in achieving highly efficient energy conversion processes. Furthermore, these are handicapped by the recycling procedures of the used nanoparticles, limited scalability, and difficult operation, which limit their simplicity and sustainability.

From the aspect of necessity for precise feature control of the nanostructure with uniform integrity and scalability in an optical reactor, the plasmonic nanogap structure leading to the plasmonic coupling between adjacent nanostructures and highly enhanced electromagnetic ( $E$ ) fields holds great potential.<sup>39</sup> The plasmonic nanogap allows for a larger absorption cross-section with a broad range of visible–infrared (vis–IR) extinction spectra.<sup>39–41</sup> As an antenna and reactor (A–R), the nanogap structure is a combined architecture where plasmonic nanogap “antennas”, acting as lenses, amplify the interaction between light and “reactor” adjacent plasmonic nanostructures. The geometric arrangement and species composition of the A–R nanostructure determine the localized or collective heat generation.<sup>42–44</sup> To date, numerous theoretical studies reported a better understanding of the plasmonic nanogap effect. Meanwhile, experimental studies have shown several probes by investigating several standard structures based on a single dimer,<sup>45–48</sup> bowtie,<sup>49–52</sup> and nano-shell structure<sup>53–56</sup> in applications focused on sensing,<sup>57–59</sup> imaging,<sup>60</sup> and photodetection.<sup>61,62</sup>

Most reported studies dealing with nanogap nanostructures have focused on the local photothermal effect. Considering that the sustainable SODIS aims scalable rapid water heating to reach the critical disinfection condition and cover a larger platform, it is necessary to achieve collective heating from the

nanogap structure to the surrounding water. The high-density and uniform plasmonic array in a large-area substrate is essential for expanding the local photothermal effect to scalable processes. Most of the current studies dealing with the plasmonic nanogap structures are still far from simultaneously achieving uniform and high-density plasmonic nanogap structure arrays with a scalable method. Despite the rapidly expanding interest and consequences on sustainable approaches outlined above, the plasmon nanogap is still in its early stage. The structural investigation and scalable integration of plasmon nanogaps for SODIS, particularly in the sub-nanometer gap region and the gap–gap interaction, are far from perfect.

In this study, we report a high-performance sustainable SODIS approach enabled by a high-density and uniform plasmonic dimer array (hPDA) integrated with the optofluidic panel (Figure 1). The integrated SODIS optofluidic panels that are expected to be equipped onto a roof in a residential place can maximize the interaction between incident light and water. The hPDA-integrated optofluidic panel, as a thermal energy storage system, results in very efficient and long-term water heating. The light-induced thermal energy generation leads to inactivation of water pathogens in the contaminated water. The highly focused electromagnetic field, as well as the highly enhanced photothermal effect of the hPDA nano-reactor and the ensuing collective heating for SODIS, result in such highly effective and sustainable performance.

The hPDA is fabricated by using a combination of block copolymer (BCP) lithography and the nanogap self-assembly. Systematic morphology and optical properties’ analysis of the plasmonic dimer’s array reveal the orderness of geometric arrangement with high density as well as uniform strong plasmonic coupling. The larger absorption cross-section and focused electric field in the plasmonic nanogap array in hPDA allow for rapid photothermal energy harvesting with high

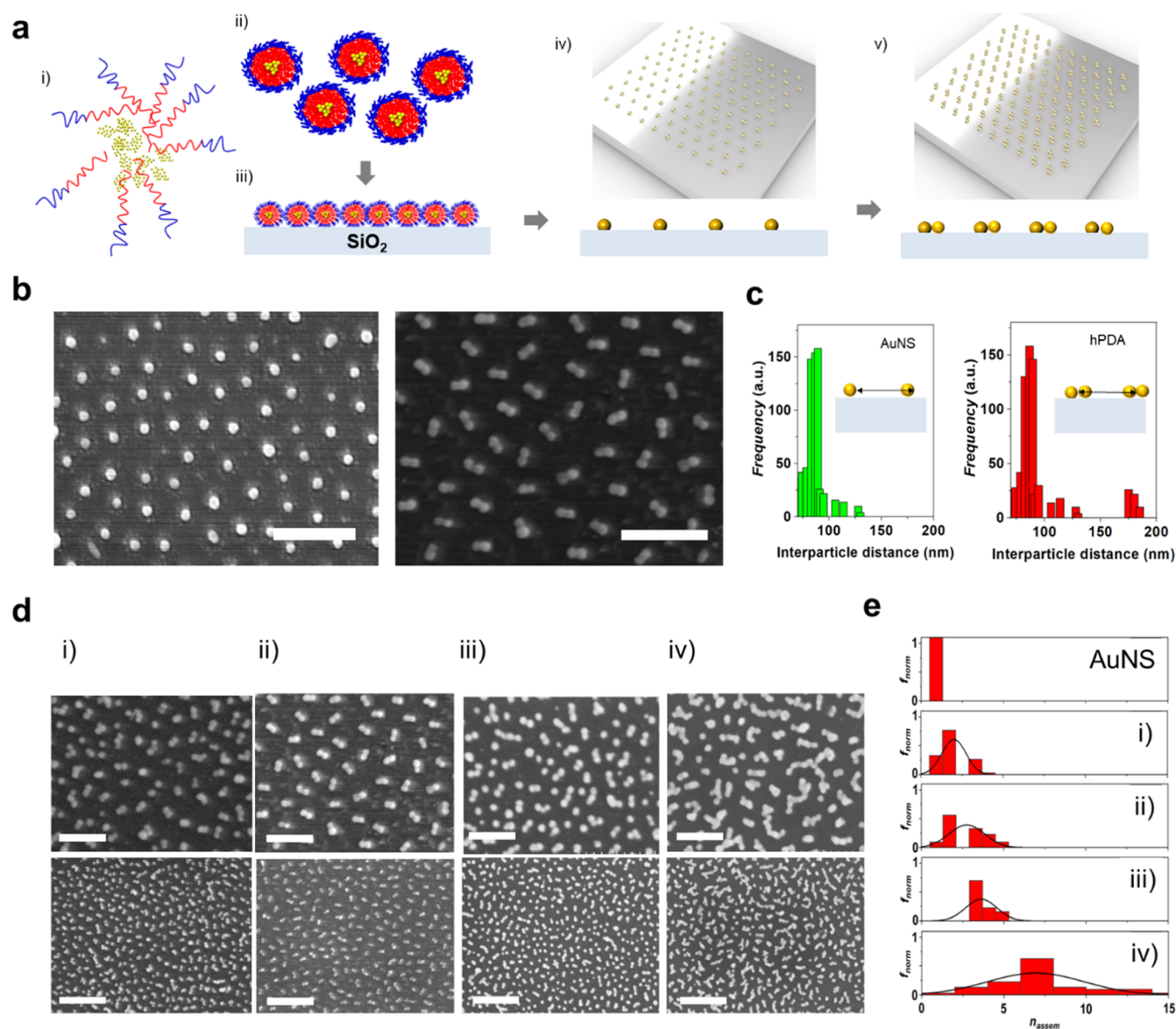


**Figure 2.** Synthesis and morphology characterization of hPDA. (a) Schematic illustration of fabrication steps of hPDA. (b) SEM images of the (i) AuNP array prepared by BCP lithography and (ii) hPDA (bridge =  $C_8$ ) (scale bars = 200 nm). The population distribution of the hPDA reveals that 91% of the 672 total particles are plasmonic dimer structures. (c) Distribution of structure–structure distances of the AuNP array and the hPDA. (d) SEM images and (e) population distribution of the plasmonic polymer array as a function of the density of additive AuNPs ( $d_{\text{AuNPs}}$ ) at (i)  $10^7$ , (ii)  $10^8$ , (iii)  $10^9$ , and (iv)  $10^{10}$  particles/mL on the first AuNP array prepared by BCP lithography (top and scale bar = 200 nm) and large-area substrates (bottom and scale bar = 500 nm).

efficiency. While many studies have been associated with the need to recycle nanoparticles, improve the performance, and increase scalable processing (Tables S1 and S2), the optofluidic reactor-integrated hPDA with larger light collection and conversion for water heating and pathogen disinfection allows for continuous water treatment and scalability to equip residential and office structures.

## RESULTS AND DISCUSSION

**Highly Ordered Plasmonic Dimer Array.** We constructed the hPDA through a combination of patterning of ordered Au nanostructure (AuNS) arrays created by BCP lithography, self-assembly of nanogaps, and subsequent assembly of secondary AuNPs (Figure 2). The BCP lithography for the first AuNS array enables highly ordered patterns on a  $\text{SiO}_2$  substrate (Figures 2a and S1). In brief, a

mixture of Au ion and a polystyrene-*block*-poly(methyl methacrylate) (PS-*b*-PMMA,  $M_n = 63$  kg/mol for PS and 142 kg/mol for PMMA) thin film was spin-coated onto a hydrophilic substrate and reduced with  $\text{O}_2$  plasma (see Methods). Subsequently, to introduce a nanogap, we functionalized the first AuNS array with thiol,  $\text{SH}(\text{CH}_2)_8\text{SH}$ , resulting in the formation of self-assembled monolayers (SAMs) of  $C_{11}$  with a thiol terminal group exposed to the exterior. Next, to form dimers, we attached AuNPs on the thiol-functionalized first AuNS array, selectively, not on the substrate. To confirm the hPDA structures, we next analyzed the morphology of the fabricated hPDA by obtaining scanning electron microscopy (SEM) images (Figures 2b and S2 and S3). We observed that the order and dimer–dimer distance of the first AuNS array were maintained as size ( $\sim 30$  nm) before/after assembling the secondary AuNP ( $\sim 40$  nm). To quantify the

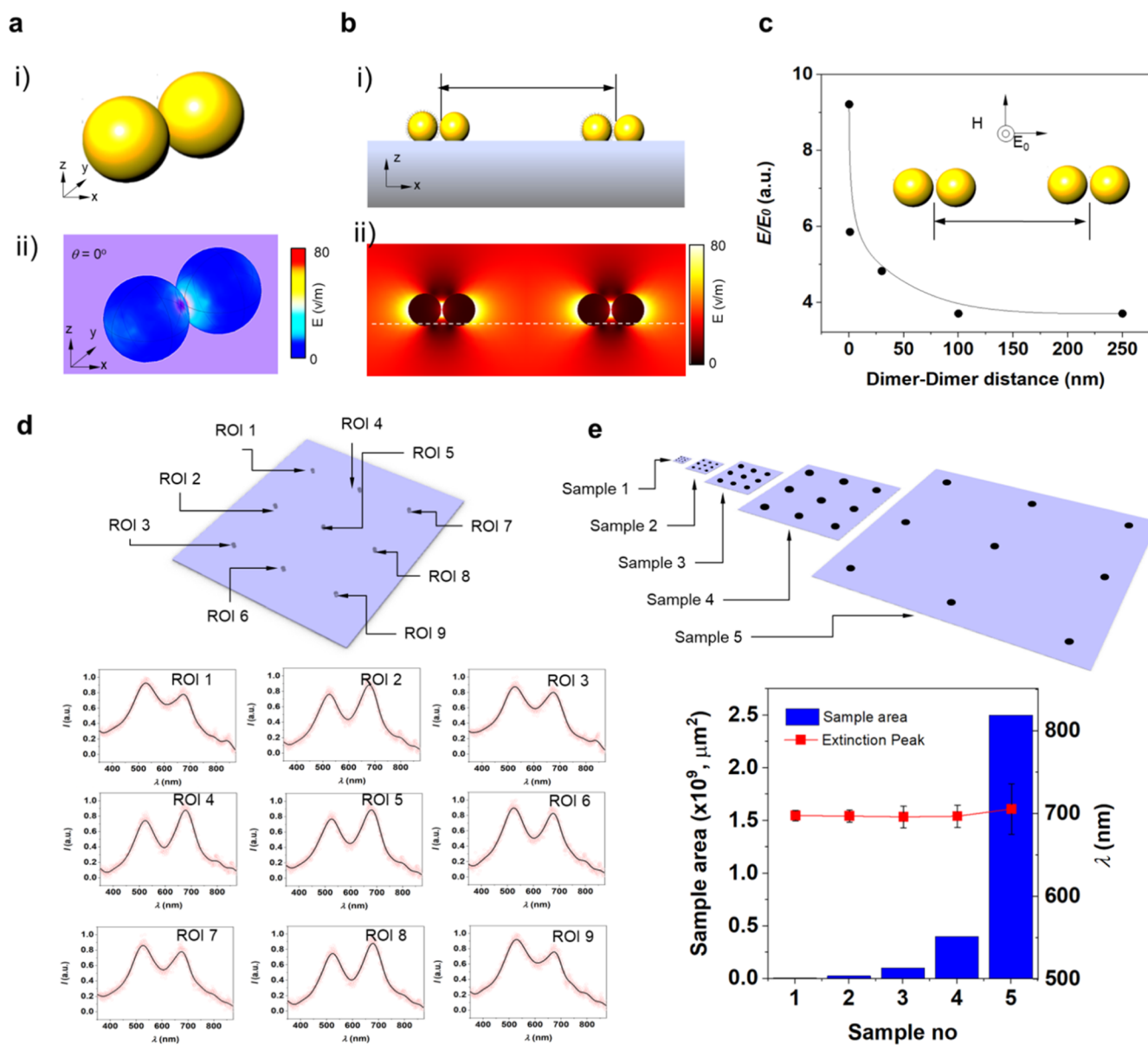


**Figure 3.** Optical properties of hPDA. (a) Schematic and (b) calculated electric field and spectra in gold dimers composed of two 30 nm gold spheres with  $d_{\text{gap}} = 1.3$  nm. (c) Schematic and electromagnetic field distribution in two dimers separated by 200 nm. Each dimer is composed of two 30 nm gold spheres with  $d_{\text{gap}} = 1.3$  nm. (d) Measured extinction spectra from nine different ROIs in a hPDA sample ( $1 \times W = 20,000 \times 20,000 \mu\text{m}^2$ ). (e) Average wavelength of the longitudinal peak in nine spots from five different substrates that have different sample areas from 0.1, 0.49, 2.5, 4.9, and 25  $\text{mm}^2$ . These data indicate that regardless of area change, the created nanogap structure shows a consistently large absorption cross-section.

yield of the dimer, we plotted the number of single and dimer structures on the substrate, respectively. In particular, around 90% of particles were dimers (Figure 2c). The density of the gold plasmonic nanostructure array can be controlled by BCP lithography. In particular, the change of the molecular weight of PS or PMMA enables us to control the size and interparticle distance. In this study, the dimer–dimer distances of the hPDA revealed a uniform distribution ( $100 \text{ nm} \pm 5\%$ ). Having this structural consistency of the hPDA after the middle of manufacturing processes, we studied the secondary AuNP effect on the shape and uniformity of the final structures. While assembling the secondary AuNPs, we changed the density of the secondary AuNPs ( $d_{\text{AuNPs}}$ ) from  $10^7$  to  $10^{10}$  particles/mL. With  $d_{\text{AuNP}}$ , the numbers of the assembled AuNP ( $n_{\text{assem}}$ ) are increased, while the uniformity decreases. For example, the

single nanoparticle is the predominant structure at  $d_{\text{AuNPs}} = 10^7$  particles/mL, while multi-nanoparticle arrays containing 4 and 10 arrays are predominant at  $10^{10}$  particles/mL (Figure 2d). Thus, the  $n_{\text{assem}}$  increased with  $d_{\text{AuNPs}}$ , while the uniformity in both the dimer–dimer distance and the  $n_{\text{assem}}$  decreased (Figure 2e).

**Strong and Uniform Light Capturing Capability on hPDA.** Having constructed the hPDA, we then characterized its light focusing capability and optical absorption (Figure 3). To analyze such features at a discrete level, we first calculated optical properties using finite element analysis (FEA) based on a boundary element method by solving Maxwell's equations (see Methods). The calculated local electric ( $E$ ) field and scattering spectrum around a single gold nanoparticle (40 nm) and a plasmonic dimer formed by 40 nm gold nanoclusters

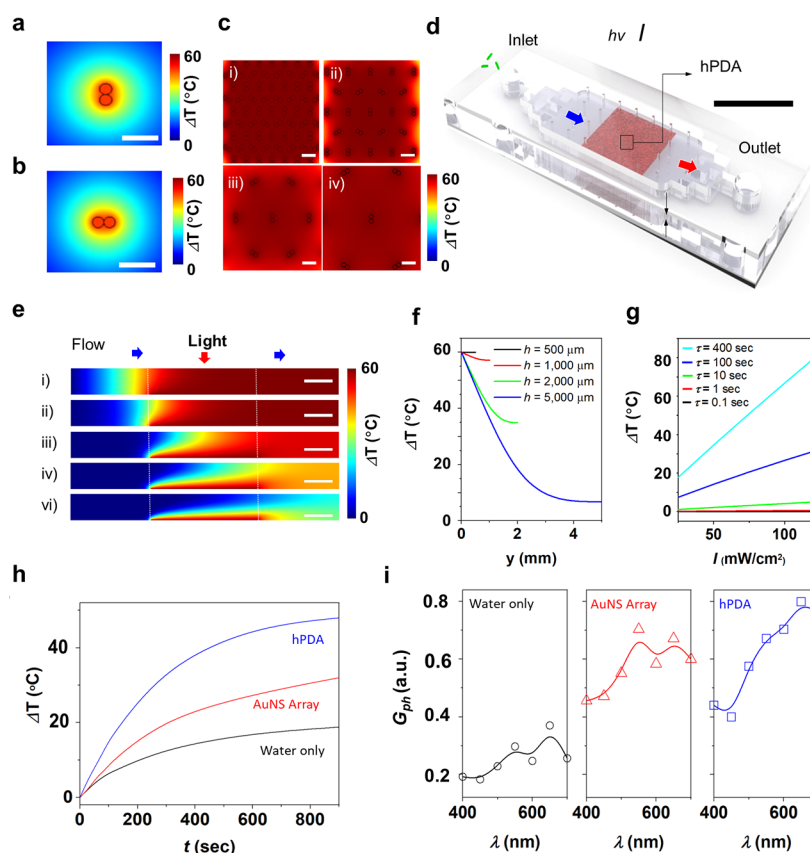


**Figure 4.** Integration of hPDA into an optofluidic reactor for the dramatically increased photothermal effect gain due to higher incident UV–vis light absorption and effective heat diffusion. Temperature distribution in a plasmonic dimer: (a) 0 and (b) 90° alignment under the incident light at 550 nm and  $I = 100 \text{ mW/cm}^2$  (scale bars = 100 nm) obtained by FEA methods. (c) Temperature distributions in hPDA with a dimer–dimer distance ( $d_{is}$ ) of (iii) 100, (iv) 450, (v) 600, and (vi) 1000 nm at  $I = 100 \text{ mW/cm}^2$  (scale bars = 100 nm) obtained by FEA methods. (d) Schematic of the integrated optofluidic reactor and key parameters; resident time of flow ( $\tau$ ), light intensity ( $I$ ), and channel height of the integrated reactor ( $h$ ). (e) Cross-sectional temperature distribution in the reactor at different  $\tau =$  (i) 10, (ii) 2, (iii) 1, (iv) 0.2, and (v) 0.1 min at  $I = 100 \text{ mW/cm}^2$  (scale bars = 100  $\mu\text{m}$ ). (f) Outlet temperature of the reactor as a function of  $h$  from 10 to 2000  $\mu\text{m}$  at  $\tau = 0.1, 0.2, 1, 2,$  and 10 min under  $I = 100 \text{ mW/cm}^2$ . (g) Outlet temperature of the reactor as a function of  $I$  from 25 to 125  $\text{mW/cm}^2$  at  $\tau = 0.1, 0.2, 1, 2,$  and 10 min with  $h = 100 \mu\text{m}$ . (h) Experimentally measured dynamic temperature gradient profile at the outlet of the reactor integrated with the hPDA and AuNP array and without nanostructures at  $I = 100 \text{ mW/cm}^2$  for  $\tau = 2$  min with  $h = 100 \mu\text{m}$ . (i) Experimentally measured temperature gradient as a function of wavelength of incident light with the hPDA and AuNP array and without nanostructures at the reactor outlet.

with a 1.3 nm long SAM (bridge =  $\text{C}_8$ )<sup>63,64</sup> layer are shown in Figure 3a. A high-intensity  $E$ -field distribution exists in the nanogap of the Au dimer. When the polarization direction is parallel to the interparticle axis, the highest  $E$ -field in the nanogap is  $\sim 20$  times greater than that of one perpendicular to the interparticle axis. In addition, the coupling effect results reveal multimodes of  $E$ -field distribution. Under perpendicular incident light (I) and (II), the  $E$ -field spectra show identical peaks at 528 and 624 nm (Figure 3b). The first peak at  $\lambda = 528$  nm is similar to that of a single AuNP, and the second one shows a larger red shift at  $\lambda = 624$  nm due to plasmonic coupling. We further performed simulation studies of the hPDA. Considering the dimer–dimer distance in the SEM images of Figure 2b, a uniform  $E$ -field distribution between dimers is observed in the built geometry (Figure 3c).

Subsequently, we experimentally characterized the optical properties of the prepared hPDA by using a dark-field microscope (see Methods) (Figure 3d). We obtained the scattering spectra of hPDA from nine separate regions of interest (ROIs) that are evenly dispersed within a 1 cm distance in the sample (width  $\times$  height = 2 cm  $\times$  2 cm) under white-light illumination. The spectra exhibit two distinct

scattering peaks regardless of the location, and these acquired spectra well matched to that of the calculated results in Figure 3b. In general, small changes to the arrangement and spacing between coupled plasmonic nanoparticles would lead to substantial changes in the absorption spectrum because the dimer–dimer distances in the SAM-assembled plasmonic dimer are within a region that should give rise to strong plasmonic coupling.<sup>65–68</sup> However, the spectrum of the constructed hPDA reveals consistency with a single dimer’s spectrum even after the construction. We further compared the area of the sample and the uniformity of the second peak. As the area of the sample increased, the location of the second peak consistently occurred around 700 nm with less than 10% deviation. This result indicates that the dimer–dimer distance in the built hPDA is uniform (Figure 3e).

**Photothermal Energy Harvesting through hPDA Integrated into an Optofluidic Reactor.** For the constructed hPDA, we investigated the photothermal effect in an integrated optofluidic reactor (Figure 4). The photothermal effect in the plasmonic dimer structure is mainly caused by three processes. First, the two nanostructures are coupled through near-field interaction. Next, due to the heat

flux generated by the neighboring nanostructure, the photothermal effect of each nanostructure was enhanced compared to that of a single nanoparticle. As the last stage, the generated heat diffused out through the nanostructures to the environment such as water and the substrate. Most of all, the generated heat power ( $P$ ) in the nanostructure directly originated from the large absorption cross-section ( $\sigma_{\text{abs}}$ ) of the plasmonic nanogap ( $P = \sigma_{\text{abs}}I$ ). The absorption power depends on the  $d_{\text{gap}}$ . The multi-physics FEA results indicate that the high  $\sigma_{\text{abs}}$  of a plasmonic dimer ( $d_{\text{gap}} = 1.3$  nm) induced large energy dissipation and led to a high-temperature gain ( $\Delta T_{\text{dimer}} = 50$  °C) compared to that ( $\Delta T_{\text{AuNP}} = 30$  °C) in a single AuNP (Figures 4a and S4). The built hPDA, according to the SEM images in Figure 2, has a uniform distribution and density. However, in the  $x$ - $y$  plane, the dimer's orientation is uneven. We used spectral analysis to explore the effect of the hPDA's uneven orientation on the photothermal effect. We plot the extinction spectra of the dimer structure ( $d_{\text{gap}} = 1.3$  nm) for perpendicular and parallel polarizations. An invariance of the absorption cross-section was observed for  $\lambda_{\text{iso}} = 537$  nm. This indicated that any incoming linearly polarized light can be split into two light beams that are cross-polarized along the structure's two primary axes. As a result, if the absorption cross-sections for the transverse and longitudinal modes are identical, increasing the polarization angle has no effect on the absorption cross-section. In other words, finding crossing sites of the transverse and longitudinal spectra is sufficient to ensure that the structure's response is polarization-angle invariant. This result indicates that for this specific wavelength, the energy absorption (and thus the temperature increase) is not dependent on the incident light polarization (Figure 4b). The presence of a nanogap does not preclude consistent heat creation as a function of light polarization, which opens the road for the application of solar optics, because the heat generation is not due to the electric field within the gap but rather with the electric field inside the metal. Due to the high thermal conductivity ( $\sim 30$  mW/K) of the Au structure, with minimal localization, this enhanced photothermal effect diffused rapidly ( $\sim$ hundreds of second)<sup>37</sup> through the structure and collective thermal diffusion occurred in the surrounding water. Such a process indicates that the plasmonic nanogap structure is an excellent approach to transform solar energy into thermal energy and store it in water in this way. The high-density and uniformly distanced array of the nanogap leads to consistent temperature profiles in a large area for the effective thermal energy storage (Figure 4c).

To test the thermal energy storage, we designed and constructed an integrated optofluidic reactor consisting of an inlet, an outlet, and an optical reaction chamber (Figures 4d, S5, and S6 and Table S3, see Methods). We integrated the hPDA on the bottom of the optical reaction chamber and characterized dynamic temperature profiles as a function of the residence time ( $\tau$ ), chamber height ( $h$ ), and light intensity ( $I$ ).

Prior to the experimental test, we performed numerical analysis to guide the range of the test conditions. In this study, for the numerical analysis of the hPDA-integrated optofluidic reactor, that is, a multiscale system involving from the nanostructure to micro opto-/thermofluidics, we performed a multi-stage simulation that is widely used for multiscale cases (Figure S5). Because the hPDA revealed good uniformity in a large area, we assumed that the whole area of the reactor's bottom has the same density of the photothermal effect at the nanoscale. With higher  $\tau$ , uniformity of temperature distribu-

tion increased (Figure 4e). Between  $\tau = 1$  and 10 min, the output temperature gain was  $\sim 50$  °C, whereas shorter  $\tau$  resulted in a lower temperature gain. In the case of  $h$ , uniform temperature distribution occurred with a shorter condition (Figure 4f). The water temperature at the chamber also increased with  $I$  (Figure 4g).

Based on these simulation results, we obtained the optimal dimension of the optical reaction chamber ( $h \times l \times W = 200 \times 10,000 \times 10,000$   $\mu\text{m}^3$ ). We then constructed the optofluidic reactor by integrating the reaction chamber made from polydimethylsiloxane (PDMS) using a soft-lithography method with the prepared hPDA substrate (see Methods). We measured the dynamic outlet temperature-gain profile of hPDA and AuNPs, respectively (Figure 4h). The measured temperature gain in hPDA ( $\Delta T_{\text{hPDA}}$ ) reached around 50 °C in  $\sim 10$  min while that ( $\Delta T_{\text{AuNP}}$ ) in the AuNP array plateaued at 30 °C in  $\sim 15$  min at the same  $I = 100$  mW/cm<sup>2</sup> and  $\tau = 400$  s. According to the differences of heat dissipation ( $Q$ ) and thermal diffusion rate between these two systems, the observed results are reasonable as shown in theory. The hPDA led to the rapid heating effect and high solar energy conversion efficiency. Furthermore, to confirm the vis/IR-induced photothermal effect in the hPDA, we characterized the photothermal energy gain ( $G_{\text{ph}}$ ) as a function of spectrum from 450 to 700 nm (Figure 4i). In this test, we used band-path filters to apply the specific wavelength. By considering the measured light intensity at each spectrum (Figures S7 and S8), we estimated  $G_{\text{ph}}$  at different wavelengths. We observed the highest value of 0.81 at 650 nm in hPDA, while the AuNP array revealed 0.63 at 550 nm at the same test condition. These trends of photothermal energy gain as a function of wavelength follow the optical properties shown in Figure 3. In addition to the nanotrimers, the longitudinal plasmon coupling band further red-shifted.<sup>69</sup> The trimer exhibits a higher absorbance overall (1%) and in the NIR region. When compared to the dimer, trimers can increase the photothermal effect. Nonetheless, it is anticipated that the influence of the trimer on the photothermal effect will not be considerable because the sun spectrum shows low irradiance as the wavelength gets longer. The optical properties are significantly affected by variations in the plasmon coupling for light polarization parallel to the first and second particle axes due to the relative geometric arrangement of the third nanoparticle in the trimer (Figure S9). To achieve constant device performance, a uniform and consistent nanotrimer array is required.

**Water Disinfection.** We performed dynamic water treatment using the integrated optofluidic reactor (Figure 5). As a representative target model, *Escherichia coli* (*E. coli*) K-12 ( $\sim 5 \times 10^6$  cfu) in a tap water-based medium (Washtenaw County, MI, USA) was used. By estimating  $-\log N / \log N_0$ , where  $N$  and  $N_0$  are the *E. coli* populations before and after the treatment, we quantified the deactivation performance and compared with them in a single AuNS array (Figure 5a). The highest *E. coli* deactivation performance occurred with hPDA, resulting in  $>5$ -log deactivation within 60 min under vis light illumination (see Methods), while *E. coli* treatment in the control (single AuNS array) results in 1.6-log inactivation. The *E. coli* deactivation with hPDA was rapid and similar to the temperature profile in Figure 4b. We also performed negative control tests under the dark condition, and 0.3-log and 0.2-log deactivation with hPDA and AuNP, respectively, were observed. In the control test, *E. coli* deactivation was higher (0.1-log) than in the treatment without nanostructures. The

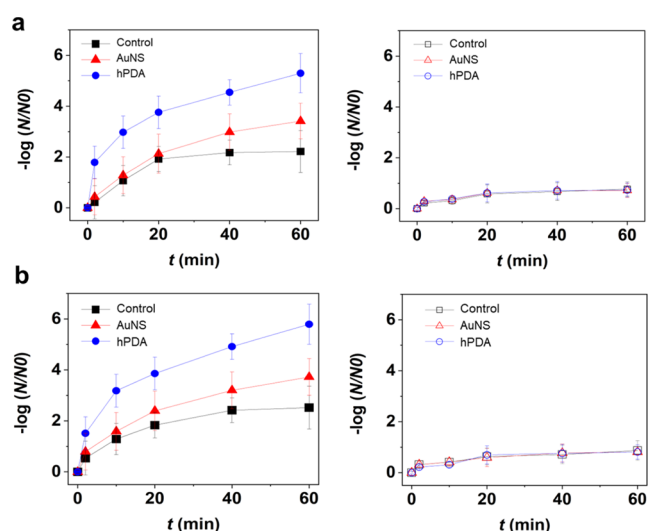


**Figure 5.** hPDA disinfection performance. Comparison of inactivation of (a) *E. coli* and (b) *Streptococcus aureus* with the AuNP array (red curve) and hPDA (blue curve) and without nanostructures (black curve) under light illumination ( $I = 100 \text{ mW/cm}^2$ ) and in the dark condition to confirm the vis photothermal effect.

surface charge effect of the AuNP was responsible for the nanostructure's considerably increased deactivation. In the case of hPDA, the nanostructure-fabricated BCP lithography was not involved in the capping agent associated with the cytotoxicity. In addition, we tested the deactivation of *Streptococcus* (Figure 5b). Unlike *E. coli*, *Streptococcus aureus* is a Gram-positive bacteria which consist of a single layered cell membrane with an outer peptidoglycan layer. After 60 min, we observed that *E. coli* inactivation showed a lower value of 5.0-log compared to 4.7-log of *Streptococcus* under the same condition. Gram-positive bacteria are more heat-resistant than Gram-negative bacteria. In *Streptococcus*, higher heat stability and the insulating effect of the peptidoglycan layer on the membrane are thought to lead to lower deactivation performance.<sup>70</sup> After the tests, we confirmed that the structural morphology of the integrated hPDA and the performance of the photothermal effect are maintained (Figure S10). Subsequently, we estimated deactivation efficiency ( $\eta_d$ ) divided by incident light intensity  $[(-\log N/\log N_0)/I_{\text{norm}}]$  as a function of wavelength (Figure S11). Between  $\lambda = 650$  and 700 nm, the highest disinfection efficiency of 3.0 occurred for the hPDA, while a single AuNS array led to a disinfection efficiency of 2.5 at  $\lambda = 550$  and 600 nm. This disinfection performance shows that high absorption cross-section of the uniform hPDA led to a strong VIS-induced enhanced photothermal effect and resulted in higher water treatment performance (Table S4). Given these performances from the hPDA-integrated optofluidic reactor, to explore the practical steps, we further conducted the disinfection tests under sunlight (AM1.5) (Figure S12). The results show that the enhanced deactivation performance of *E. coli* and *Streptococcus* resulting in  $>5$ -log deactivation within 60 min still occurs.

## CONCLUSIONS

In conclusion, we have demonstrated a sustainable water treatment by integrating the hPDA and the optofluidic reactor. The hPDA was created using a combination of BCP lithography and secondary AuNP assembly approaches. The dimer array resulted in significantly improved visible/IR

harvesting as well as high-efficiency thermal energy conversion. Subsequently, we demonstrated a 5-fold increased water pathogen disinfection efficiency. For the sustainable water treatment and solar energy storage, we showed that the uniform array of plasmonic dimers in the microfluidic reactor is a key design feature of the optofluidic reactor. In addition, this enabled us to create the decentralized point-of-use platform that requires the straightforward device integration and assembly strategy and the repeated operation without particle separation processes. A further scale-up study of the integrated optofluidic reactor by increasing the dimension and the capacity of water flow is needed to achieve the next stage. For the practical application of the optofluidic reactor that integrated with hPDA, blockage can occur. Gray water contains biological contaminants with several types of ions such as potassium, calcium, magnesium, and zinc ion content, which can clog the reactor system. By combining clogging-free approaches including the salt-rejecting techniques.<sup>71–74</sup> Such a high-throughput optofluidic reactor could be implemented in residential/office building structures, thereby facilitating decentralized energy harvesting and water as sustainable methods.

## METHODS

**Chemicals.** 1,8-Octanedithiol ( $>97\%$ ), ethanol ( $\geq 99.9\%$ ), gold(III) chloride trihydrate ( $\geq 99.9\%$ ), sodium citrate tribasic dehydrate ( $\geq 99.0\%$ ), HCl (37%), and toluene (99.5%) were purchased from Sigma-Aldrich. PS-*b*-poly(2-vinylpyridine) (PS-*b*-P2VP) (S units: 213,000; VP units: 153,000) was purchased from Polymer Science. The PDMS elastomer and curing agent were purchased from Corning. Nano-pure deionized (DI) water ( $18.1 \text{ M}\Omega \text{ cm}$ ) was produced in-house.

**Preparation of a Uniform and High-Density Gold Nanostructure Array.** A uniform and high-density gold plasmonic nanoantenna array was prepared using BCP nanolithography, as previously reported.<sup>75,76</sup> We dissolved PS-*b*-P2VP (S units: 213,000; VP units: 153,000) in toluene at a concentration of 4 mg/mL and stirred this solution overnight. Then, gold(III) chloride trihydrate powder with a molar ratio of 0.4 per vinyl pyridine unit was added and stirred for 72 h. Next, we transferred the Au-BCP micelles as a uniform monolayer onto a silicon substrate by spin-coating. Next, the substrate was treated with  $\text{O}_2$  plasma ( $P = 500 \text{ W}$ , 0.3 mbar) for 30 min. After all processes, we confirmed the morphology using a scanning electron microscope (Hitachi SU8000).

**Preparation of a Dimer Array.** After generating a SAM layer on the primary AuNS array, AuNPs were selectively connected (Figures 2 and S1) (see Supporting Information). Briefly, we immersed the primary AuNS array substrates in an ethanol solution of the thiol (1-octanethiol, 1 mM, 1 mL) for 16 h for the formation of thermodynamically stable SAMs. After washing the functionalized substrate, we incubated it in the AuNP colloidal solution ( $10^8 \text{ pM}$ , 2 mL) for 3 h. The substrates were washed with water and dried with  $\text{N}_2$ .

**Characterization of the hPDA.** We confirmed the structural/optical properties of the fabricated hPDA. First, we obtained SEM images of the fabricated hPDA (see Supporting Information). The density, uniformity, and size distribution of the fabricated nanostructure array were analyzed by ImageJ. To characterize the optical properties of the fabricated and prepared hPDA, we used a single particle dark-field (DF) microscope (Olympus IX-71). With a 40 $\times$  objective (Olympus UPLFLN), the sample was imaged onto a camera and with a spectrometer (Pixis with Princeton instrument Spectro Pro).

**Numerical Analysis of the Integrated Optofluidic Reactor.** In order to investigate the effect of geometry on the design of the integrated optofluidic reactor, we performed FEA (COMSOL Multiphysics software) (see details in Supporting Information). We

solved Navier–Stokes and continuity equations to analyze fluidic profiles, assuming that the flow is laminar and in steady-state

$$\rho(\mathbf{u} \cdot \nabla) \mathbf{u} = -\nabla p + \mu \nabla^2 \mathbf{u} - \frac{2}{3} \mu \nabla(\nabla \cdot \mathbf{u}) \quad (1)$$

$$\nabla \cdot (\rho \mathbf{u}) = 0 \quad (2)$$

where  $\rho$ ,  $\mu$ ,  $p$ , and  $\mathbf{u}$  are the density, the dynamic viscosity, the pressure, and velocity vectors of the fluid, respectively. The thermal energy flow in the system is estimated by solving the conduction and convection heat transfer equation.

$$\rho c_p \mathbf{u} \cdot \nabla T = \nabla \cdot (k \cdot T) + Q \quad (3)$$

where  $c_p$ ,  $T$ ,  $k$ , and  $Q$  are the specific heat of the water, the thermal conductivity, temperature, and the heat source, respectively.

**Integrated Optofluidic Reactor.** We constructed the integrated optofluidic reactor using previously reported methods.<sup>18</sup> We designed and integrated microflow distributors between the inlet and the reaction chamber, as well as between the output and the reaction chamber, to achieve a uniform flow distribution. After preparing the hPDAs on a substrate and microfluidic chamber individually, we assembled them along the alignment marks (see [Supporting Information](#)).

**Photothermal Energy Harvesting Test.** We estimated the photothermal activity in the optofluidic reactor under light illumination [Dolan-Jenner Fiber-Lite 180 with a 150 W, 21 V halogen (EKE) lamp] (see [Supporting Information](#)). The flow rate of the solution into an optofluidic reactor was controlled by using a syringe pump (Cole Palmer, EW-74900-00). The temperature of the solution was monitored in real time by a type-K insulated thermocouple, purchased from OMEGA engineering (part number SSC-TT-K-40-36). A National Instrument (NI) 9213 16-channel thermocouple module with a high-speed mode, auto zero, and cold junction compensation was used for accurate temperature acquisition from the thermocouple. We maintained environmental temperature at 25 °C using a water circulator. The photothermal energy gain is defined as  $G_{\text{ph}} = c_p \dot{m} \Delta T / IA$ , where  $\dot{m}$ ,  $\Delta T$ ,  $I$ , and  $A$  are the mass flow rate of water in the integrated optofluidic reactor, the temperature difference between the inlet and outlet, the light intensity, and the area of the reactor, respectively.

**Water Disinfection Test.** The cultured bacteria were added to 10 mL of Luria–Bertani (LB) broth and incubated (see [Supporting Information](#)). Using an OD meter, a portion of the solution containing the bacteria was diluted to  $\sim 5 \times 10^6$  cfu/mL with tap water. Under light illumination, we flowed the prepared *E. coli* sample in the reactor and collected the treated *E. coli* solution through the outlet of the optofluidic reactor to a microtube. We quantified the number of inactivated *E. coli* using a standard spread-plate counting method.

**Finite Element Analysis.** We investigated the electromagnetic fields around hPDA using FEA (COMSOL Multiphysics). The nanostructure was discretized by spheres with 1444 vertices, a diameter of 40 nm, and an interparticle separation of 1 nm based on the linker molecule length. The dielectric function for the gold nanoparticles was taken from Johnson and Christy,<sup>77</sup> the average dielectric constant of the environment was assumed as 1.33. We assumed perfect absorption at the outer boundary to minimize reflections by setting a perfectly matched layer and an integration layer in concentric space. We decided the size of the hPDA according to the obtained SEM images of hPDA.

## ■ ASSOCIATED CONTENT

### SI Supporting Information

The Supporting Information is available free of charge at <https://pubs.acs.org/doi/10.1021/acsnm.3c00026>.

Detailed materials and experimental section, comparison of nanostructures and their systems for solar water disinfection, comparison of fabrication methods for

nanogaps, boundary conditions for multiphysics simulations in the optofluidic reactor, method of nanostructure construction, additional SEM images of the AuNS array and hPDA with a wide field of views, yields of hPDA and control sample, flow chart of numerical analysis for the multi-scaled integrated optofluidic reactor, optofluidic reactor design and computational structure of the optofluidic reactor, constructed optofluidic reactor, spectrum of light source, optical filters at the individual wavelength and source intensity, comparison of temperature gradients in nanostructures, structural durability of the integrated hPDA with the optofluidic reactor, water pathogen inactivation efficiency as a function of wavelength, and hPDA disinfection performance ([PDF](#))

## ■ AUTHOR INFORMATION

### Corresponding Authors

**Somin Eunice Lee** – Department of Electrical & Computer Engineering, Department of Biomedical Engineering, Department of Applied Physics, and Macromolecular Science & Engineering Program, University of Michigan at Ann Arbor, Ann Arbor, Michigan 48109, United States; Biointerfaces Institute, University of Michigan, Ann Arbor, Michigan 48109, United States; Phone: (734) 764-7054; Email: [slee@umich.edu](mailto:slee@umich.edu)

**Younggeun Park** – Department of Mechanical Engineering, University of Michigan at Ann Arbor, Ann Arbor, Michigan 48109, United States; Weil Institute for Critical Care Research and Innovation, University of Michigan, Ann Arbor, Michigan 48109, United States; [orcid.org/0000-0002-8346-6142](https://orcid.org/0000-0002-8346-6142); Phone: (734) 936-2410; Email: [ygpark@umich.edu](mailto:ygpark@umich.edu)

### Authors

**Daniel Krueger** – Department of Chemical Engineering, University of Michigan at Ann Arbor, Ann Arbor, Michigan 48109, United States

**Ashley Graves** – Department of Chemical Engineering, University of Michigan at Ann Arbor, Ann Arbor, Michigan 48109, United States; Department of Chemistry, University of Michigan at Ann Arbor, Ann Arbor, Michigan 48109, United States

**Yanan Chu** – Department of Electrical & Computer Engineering, University of Michigan at Ann Arbor, Ann Arbor, Michigan 48109, United States

**Jianhan Pan** – Department of Electrical & Computer Engineering, University of Michigan at Ann Arbor, Ann Arbor, Michigan 48109, United States

Complete contact information is available at: <https://pubs.acs.org/doi/10.1021/acsnm.3c00026>

### Notes

The authors declare no competing financial interest.

## ■ ACKNOWLEDGMENTS

This research was supported by the academic research fund and Mcubed at the University of Michigan, the National Science Foundation (ECE 1454188), and the Air Force Office of Scientific Research (AFOSR FA9550-16-1-0272, FA9550-19-1-0186, FA9550-22-1-0285).

## REFERENCES

- (1) UNESCO. *UN World Water Development Report (WWDR4)*, 2012; Vol. 4.
- (2) UN-Water *The United Nations World Water Development Report 3—Water in a Changing World*; UNESCO Publishing/Earthscan, 2009.
- (3) Clasen, T.; Haller, L.; Walker, D.; Bartram, J.; Cairncross, S. Cost-effectiveness of water quality interventions for preventing diarrhoeal disease in developing countries. *J. Water Health* **2007**, *5*, 599–608.
- (4) Westerhoff, P.; Alvarez, P.; Li, Q.; Gardea-Torresdey, J.; Zimmerman, J. Overcoming implementation barriers for nanotechnology in drinking water treatment. *Environ. Sci.: Nano* **2016**, *3*, 1241–1253.
- (5) McGuigan, K. G.; Conroy, R. M.; Mosler, H.-J.; Preez, M. d.; Ubomba-Jaswa, E.; Fernandez-Ibañez, P. Solar water disinfection (SODIS): A review from bench-top to roof-top. *J. Hazard. Mater.* **2012**, *235–236*, 29–46.
- (6) Fisher, M. B.; Iriarte, M.; Nelson, K. L. Solar water disinfection (SODIS) of *Escherichia coli*, *Enterococcus* spp., and MS2 coliphage: Effects of additives and alternative container materials. *Water Res.* **2012**, *46*, 1745–1754.
- (7) Mauter, M. S.; Zucker, I.; Perreault, F.; Werber, J. R.; Kim, J.-H.; Elimelech, M. The role of nanotechnology in tackling global water challenges. *Nat. Sustain.* **2018**, *1*, 166–175.
- (8) Wang, L.; Feng, Y.; Wang, K.; Liu, G. Solar water sterilization enabled by photothermal nanomaterials. *Nano Energy* **2021**, *87*, 106158.
- (9) Govorov, A. O.; Zhang, W.; Skeini, T.; Richardson, H.; Lee, J.; Kotov, N. A. Gold nanoparticle ensembles as heaters and actuators: melting and collective plasmon resonances. *Nanoscale Res. Lett.* **2006**, *1*, 84.
- (10) Fei Guo, C.; Sun, T.; Cao, F.; Liu, Q.; Ren, Z. Metallic nanostructures for light trapping in energy-harvesting devices. *Light: Sci. Appl.* **2014**, *3*, No. e161.
- (11) Loeb, S.; Li, C.; Kim, J.-H. Solar Photothermal Disinfection using Broadband-Light Absorbing Gold Nanoparticles and Carbon Black. *Environ. Sci. Technol.* **2018**, *52*, 205–213.
- (12) Lee, S. E.; Sasaki, D. Y.; Park, Y.; Xu, R.; Brennan, J. S.; Bissell, M. J.; Lee, L. P. Photonic Gene Circuits by Optically Addressable siRNA-Au Nanoantennas. *ACS Nano* **2012**, *6*, 7770–7780.
- (13) Lee, S. E.; Liu, G. L.; Kim, F.; Lee, L. P. Remote Optical Switch for Localized and Selective Control of Gene Interference. *Nano Lett.* **2009**, *9*, 562–570.
- (14) Liu, Y.; Park, Y.; Lee, S. E. Thermo-responsive mechano-optical plasmonic nano-antenna. *Appl. Phys. Lett.* **2016**, *109* (1), 013109.
- (15) Jiang, R.; Cheng, S.; Shao, L.; Ruan, Q.; Wang, J. Mass-Based Photothermal Comparison Among Gold Nanocrystals, PbS Nanocrystals, Organic Dyes, and Carbon Black. *J. Phys. Chem. C* **2013**, *117*, 8909–8915.
- (16) Nikitin, A. Y.; Guinea, F.; Garcia-Vidal, F. J.; Martin-Moreno, L. Surface plasmon enhanced absorption and suppressed transmission in periodic arrays of graphene ribbons. *Phys. Rev. B: Condens. Matter Mater. Phys.* **2012**, *85*, 081405.
- (17) Qu, X.; Alvarez, P. J.; Li, Q. Applications of nanotechnology in water and wastewater treatment. *Water Res.* **2013**, *47*, 3931–3946.
- (18) Murphy, E.; Liu, Y.; Krueger, D.; Prasad, M.; Lee, S. E.; Park, Y. Visible-Light Induced Sustainable Water Treatment Using Plasmosemiconductor Nanogap Bridge Array, PNA. *Small* **2021**, *17*, 2006044.
- (19) Naldoni, A.; Shalaev, V. M.; Brongersma, M. L. Applying plasmonics to a sustainable future. *Science* **2017**, *356*, 908–909.
- (20) Da, A.; Chu, Y.; Krach, J.; Liu, Y.; Park, Y.; Lee, S. E. Optical Penetration of Shape-Controlled Metallic Nanosensors across Membrane Barriers. *Sensors* **2023**, *23* (5), 2824.
- (21) Cui, G.; Liu, Y.; Zu, D.; Zhao, X.; Zhang, Z.; Kim, D. Y.; Senaratne, P.; Fox, A.; Sept, D.; Park, Y. Opening long-time investigation window of living matter by nonbleaching phase intensity nanoscope: PINE. *arXiv*, 2023.
- (22) Zhang, Z.; Jeong, H.; Zu, D.; Zhao, X.; Senaratne, P.; Filbin, J.; Silber, B.; Kang, S.; Gladstone, A.; Lau, M.; Cui, G.; Park, Y.; Lee, S. E. Dynamic observations of CRISPR-Cas target recognition and cleavage heterogeneities. *Nanophotonics* **2022**, *11* (19), 4419–4425.
- (23) Park, Y.; Yoon, H. J.; Lee, S. E.; Lee, L. P. Multifunctional cellular targeting, molecular delivery, and imaging by integrated mesoporous-silica with optical nanocrescent antenna: MONA. *ACS Nano* **2022**, *16* (2), 2013–2023.
- (24) Liu, Y.; Zu, D.; Zhang, Z.; Zhao, X.; Cui, G.; Hentschel, M.; Park, Y.; Lee, S. E. Rapid Depolarization-Free Nanoscopic Background Elimination of Cellular Metallic Nanoprobes. *Advanced Intelligent Systems* **2022**, *4* (11), 2200180.
- (25) Saha, T.; Mondal, J.; Khiste, S.; Lusic, H.; Hu, Z.-W.; Jayabalan, R.; Hodgetts, K. J.; Jang, H.; Sengupta, S.; Lee, S. E.; Park, Y.; Lee, L. P.; Goldman, A. Nanotherapeutic approaches to overcome distinct drug resistance barriers in models of breast cancer. *Nanophotonics* **2021**, *10* (12), 3063–3073.
- (26) Liu, Y.; Zhang, Z.; Park, Y.; Lee, S. E. Ultraprecision imaging and manipulation of plasmonic nanostructures by integrated nanoscopic correction. *Small* **2021**, *17* (21), 2007610.
- (27) Lin, W. K.; Cui, G.; Burns, Z.; Zhao, X.; Liu, Y.; Zhang, Z.; Wang, Y.; Ye, X.; Park, Y.; Lee, S. E. Optically and Structurally Stabilized Plasmobio Interlinking Networks. *Advanced Materials Interfaces* **2021**, *8* (1), 2001370.
- (28) Lee, S. E.; Chen, Q.; Bhat, R.; Petkiewicz, S.; Smith, J. M.; Ferry, V. E.; Correia, A. L.; Alivisatos, A. P.; Bissell, M. J. Reversible aptamer-Au plasmon rulers for secreted single molecules. *Nano Letters* **2015**, *15* (7), 4564–4570.
- (29) Lee, S. E.; Alivisatos, A. P.; Bissell, M. J. Toward plasmonics-enabled spatiotemporal activity patterns in three-dimensional culture models. *Systems Biomedicine* **2013**, *1* (1), 12–19.
- (30) Lee, S. E.; Lee, L. P. Biomolecular plasmonics for quantitative biology and nanomedicine. *Current Opinion in Biotechnology* **2010**, *21* (4), 489–497.
- (31) Lee, S. E.; Lee, L. P. Nanoplasmonic gene regulation. *Current Opinion in Chemical Biology* **2010**, *14* (5), 623–633.
- (32) Lee, S. E.; Sasaki, D. Y.; Perroud, T. D.; Yoo, D.; Patel, K. D.; Lee, L. P. Biologically functional cationic phospholipid-gold nanoplasmonic carriers of RNA. *J. Am. Chem. Soc.* **2009**, *131* (39), 14066–14074.
- (33) Zhou, L.; Tan, Y.; Wang, J.; Xu, W.; Yuan, Y.; Cai, W.; Zhu, S.; Zhu, J. 3D self-assembly of aluminium nanoparticles for plasmon-enhanced solar desalination. *Nat. Photonics* **2016**, *10*, 393–398.
- (34) Neumann, O.; Urban, A. S.; Day, J.; Lal, S.; Nordlander, P.; Halas, N. J. Solar Vapor Generation Enabled by Nanoparticles. *ACS Nano* **2013**, *7*, 42–49.
- (35) Gao, M.; Zhu, L.; Peh, C. K.; Ho, G. W. Solar absorber material and system designs for photothermal water vaporization towards clean water and energy production. *Energy Environ. Sci.* **2019**, *12*, 841–864.
- (36) Jauffred, L.; Samadi, A.; Klingberg, H.; Bendix, P. M.; Oddershede, L. B. Plasmonic Heating of Nanostructures. *Chem. Rev.* **2019**, *119*, 8087–8130.
- (37) Keblinski, P.; Cahill, D. G.; Bodapati, A.; Sullivan, C. R.; Taton, T. A. Limits of localized heating by electromagnetically excited nanoparticles. *J. Appl. Phys.* **2006**, *100*, 054305.
- (38) Kim, M.; Lee, J.-H.; Nam, J.-M. Plasmonic Photothermal Nanoparticles for Biomedical Applications. *Adv. Sci.* **2019**, *6*, 1900471.
- (39) Nordlander, P.; Oubre, C.; Prodan, E.; Li, K.; Stockman, M. I. Plasmon Hybridization in Nanoparticle Dimers. *Nano Lett.* **2004**, *4*, 899–903.
- (40) Rechberger, W.; Hohenau, A.; Leitner, A.; Krenn, J. R.; Lamprecht, B.; Aussenegg, F. R. Optical properties of two interacting gold nanoparticles. *Opt. Commun.* **2003**, *220*, 137–141.
- (41) Su, K. H.; Wei, Q. H.; Zhang, X.; Mock, J. J.; Smith, D. R.; Schultz, S. Interparticle Coupling Effects on Plasmon Resonances of Nanogold Particles. *Nano Lett.* **2003**, *3*, 1087–1090.
- (42) Dongare, P. D.; Zhao, Y.; Renard, D.; Yang, J.; Neumann, O.; Metz, J.; Yuan, L.; Alabastri, A.; Nordlander, P.; Halas, N. J. A 3D

Plasmonic Antenna-Reactor for Nanoscale Thermal Hotspots and Gradients. *ACS Nano* **2021**, *15*, 8761–8769.

(43) Khosravi Khorashad, L.; Besteiro, L. V.; Wang, Z.; Valentine, J.; Govorov, A. O. Localization of Excess Temperature Using Plasmonic Hot Spots in Metal Nanostructures: Combining Nano-Optical Antennas with the Fano Effect. *J. Phys. Chem. C* **2016**, *120*, 13215–13226.

(44) Zhou, L.; Swearer, D. F.; Zhang, C.; Robotjazi, H.; Zhao, H.; Henderson, L.; Dong, L.; Christopher, P.; Carter, E. A.; Nordlander, P.; Halas, N. J. Quantifying hot carrier and thermal contributions in plasmonic photocatalysis. *Science* **2018**, *362*, 69–72.

(45) Scholl, J. A.; García-Etxarri, A.; Koh, A. L.; Dionne, J. A. Observation of Quantum Tunneling between Two Plasmonic Nanoparticles. *Nano Lett.* **2013**, *13*, 564–569.

(46) Savage, K. J.; Hawkeye, M. M.; Esteban, R.; Borisov, A. G.; Aizpurua, J.; Baumberg, J. J. Revealing the quantum regime in tunnelling plasmonics. *Nature* **2012**, *491*, 574.

(47) Tan, S. F.; Wu, L.; Yang, J. K. W.; Bai, P.; Bosman, M.; Nijhuis, C. A. Quantum Plasmon Resonances Controlled by Molecular Tunnel Junctions. *Science* **2014**, *343*, 1496–1499.

(48) Zhu, W.; Crozier, K. B. Quantum mechanical limit to plasmonic enhancement as observed by surface-enhanced Raman scattering. *Nat. Commun.* **2014**, *5*, 5228.

(49) Morshed, M.; Khaleque, A.; Hattori, H. T. Multi-layered bowtie nano-antennas. *J. Appl. Phys.* **2017**, *121*, 133106.

(50) Hatab, N. A.; Hsueh, C.-H.; Gaddis, A. L.; Retterer, S. T.; Li, J.-H.; Eres, G.; Zhang, Z.; Gu, B. Free-Standing Optical Gold Bowtie Nanoantenna with Variable Gap Size for Enhanced Raman Spectroscopy. *Nano Lett.* **2010**, *10*, 4952–4955.

(51) Yu, N.; Cubukcu, E.; Diehl, L.; Bour, D.; Corzine, S.; Zhu, J.; Höfler, G.; Crozier, K. B.; Capasso, F. Bowtie plasmonic quantum cascade laser antenna. *Opt. Express* **2007**, *15*, 13272–13281.

(52) Fromm, D. P.; Sundaramurthy, A.; Schuck, P. J.; Kino, G.; Moerner, W. E. Gap-Dependent Optical Coupling of Single “Bowtie” Nanoantennas Resonant in the Visible. *Nano Lett.* **2004**, *4*, 957–961.

(53) Radloff, C.; Halas, N. J. Plasmonic Properties of Concentric Nanoshells. *Nano Lett.* **2004**, *4*, 1323–1327.

(54) Tuersun, P.; Han, X. e. Optical absorption analysis and optimization of gold nanoshells. *Appl. Opt.* **2013**, *52*, 1325–1329.

(55) Prodan, E.; Radloff, C.; Halas, N. J.; Nordlander, P. A Hybridization Model for the Plasmon Response of Complex Nanostructures. *Science* **2003**, *302*, 419–422.

(56) Jørgensen, J. T.; Norregaard, K.; Tian, P.; Bendix, P. M.; Kjaer, A.; Oddershede, L. B. Single Particle and PET-based Platform for Identifying Optimal Plasmonic Nano-Heaters for Photothermal Cancer Therapy. *Sci. Rep.* **2016**, *6*, 30076.

(57) Jin, H. M.; Kim, J. Y.; Heo, M.; Jeong, S.-J.; Kim, B. H.; Cha, S. K.; Han, K. H.; Kim, J. H.; Yang, G. G.; Shin, J.; Kim, S. O. Ultralarge Area Sub-10 nm Plasmonic Nanogap Array by Block Copolymer Self-Assembly for Reliable High-Sensitivity SERS. *ACS Appl. Mater. Interfaces* **2018**, *10*, 44660–44667.

(58) Jiang, J.; Wang, X.; Li, S.; Ding, F.; Li, N.; Meng, S.; Li, R.; Qi, J.; Liu, Q.; Liu, G. L. Plasmonic nano-arrays for ultrasensitive biosensing. *Nanophotonics* **2018**, *7*, 1517–1531.

(59) Kubo, W.; Fujikawa, S. Au Double Nanopillars with Nanogap for Plasmonic Sensor. *Nano Lett.* **2011**, *11*, 8–15.

(60) Farmakidis, N.; Youngblood, N.; Li, X.; Tan, J.; Swett, J. L.; Cheng, Z.; Wright, C. D.; Pernice, W. H. P.; Bhaskaran, H. Plasmonic nanogap enhanced phase-change devices with dual electrical-optical functionality. *Sci. Adv.* **2019**, *5*, No. eaaw2687.

(61) Ge, J.; Luo, M.; Zou, W.; Peng, W.; Duan, H. Plasmonic photodetectors based on asymmetric nanogap electrodes. *Appl. Phys. Express* **2016**, *9*, 084101.

(62) Shi, S. F.; Xu, X.; Ralph, D. C.; McEuen, P. L. Plasmon Resonance in Individual Nanogap Electrodes Studied Using Graphene Nanoconstrictions as Photodetectors. *Nano Lett.* **2011**, *11*, 1814–1818.

(63) Jung, H.; Cha, H.; Lee, D.; Yoon, S. Bridging the Nanogap with Light: Continuous Tuning of Plasmon Coupling between Gold Nanoparticles. *ACS Nano* **2015**, *9*, 12292–12300.

(64) Cha, H.; Yoon, J. H.; Yoon, S. Probing Quantum Plasmon Coupling Using Gold Nanoparticle Dimers with Tunable Interparticle Distances Down to the Subnanometer Range. *ACS Nano* **2014**, *8*, 8554–8563.

(65) Liu, Y.; Zhang, Z.; Park, Y.; Lee, S. E. Ultraprecision Imaging and Manipulation of Plasmonic Nanostructures by Integrated Nanoscopic Correction. *Small* **2021**, *17*, 2007610.

(66) Artar, A.; Yanik, A. A.; Altug, H. Directional Double Fano Resonances in Plasmonic Hetero-Oligomers. *Nano Lett.* **2011**, *11*, 3694–3700.

(67) Bao, K.; Mirin, N. A.; Nordlander, P. Fano resonances in planar silver nanosphere clusters. *Appl. Phys. A* **2010**, *100*, 333–339.

(68) Lassiter, J. B.; Sobhani, H.; Knight, M. W.; Mielczarek, W. S.; Nordlander, P.; Halas, N. J. Designing and Deconstructing the Fano Lineshape in Plasmonic Nanoclusters. *Nano Lett.* **2012**, *12*, 1058–1062.

(69) Lee, D.; Yoon, S. Gold Nanotrimers: A Preparation Method and Optical Responses. *Bull. Korean Chem. Soc.* **2016**, *37*, 987–988.

(70) Jay, J. M.; Loessner, M. J.; Golden, D. A. Food Protection with High Temperatures, and Characteristics of Thermophilic Microorganisms. In *Modern Food Microbiology*; Jay, J. M., Loessner, M. J., Golden, D. A., Eds.; Springer US: Boston, MA, 2005; pp 415–441.

(71) Liu, G.; Chen, T.; Xu, J.; Yao, G.; Xie, J.; Cheng, Y.; Miao, Z.; Wang, K. Salt-Rejecting Solar Interfacial Evaporation. *Cell Rep. Phys. Sci.* **2021**, *2*, 100310.

(72) Huang, Y.-X.; Wang, Z.; Jin, J.; Lin, S. Novel Janus Membrane for Membrane Distillation with Simultaneous Fouling and Wetting Resistance. *Environ. Sci. Technol.* **2017**, *51*, 13304–13310.

(73) Guo, X.; Gao, H.; Wang, S.; Yin, L.; Dai, Y. Scalable, flexible and reusable graphene oxide-functionalized electrospun nanofibrous membrane for solar photothermal desalination. *Desalination* **2020**, *488*, 114535.

(74) Finnerty, C.; Zhang, L.; Sedlak, D. L.; Nelson, K. L.; Mi, B. Synthetic Graphene Oxide Leaf for Solar Desalination with Zero Liquid Discharge. *Environ. Sci. Technol.* **2017**, *51*, 11701–11709.

(75) Davidi, I.; Patra, D.; Hermida-Merino, D.; Portale, G.; Rotello, V. M.; Raviv, U.; Shenhar, R. Hierarchical Structures of Polystyrene-block-poly(2-vinylpyridine)/Palladium–Pincer Surfactants: Effect of Weak Surfactant–Polymer Interactions on the Morphological Behavior. *Macromolecules* **2014**, *47*, 5774–5783.

(76) Mistark, P. A.; Park, S.; Yalcin, S. E.; Lee, D. H.; Yavuzcetin, O.; Tuominen, M. T.; Russell, T. P.; Achermann, M. Block-Copolymer-Based Plasmonic Nanostructures. *ACS Nano* **2009**, *3*, 3987–3992.

(77) Johnson, P. B.; Christy, R. W. Optical Constants of the Noble Metals. *Phys. Rev. B: Solid State* **1972**, *6*, 4370–4379.